Title
Multiscale Computational Analysis of Right Ventricular Mechanoenergetics

Journal
Journal of Biomechanical Engineering, 140(8)

ISSN
0148-0731

Authors
Pewowaruk, Ryan J
Philip, Jennifer L
Tewari, Shivendra G
et al.

Publication Date
2018-08-01

DOI
10.1115/1.4040044

Peer reviewed

Ryan J. Pewowaruk
Mem. ASME
Biomedical Engineering,
University of Wisconsin—Madison,
2145 Engineering Centers Building,
1550 Engineering Drive,
Madison, WI 53706
e-mail: pewowaruk@wisc.edu

Jennifer L. Philip
Surgery,
University of Wisconsin—Madison,
2143 Engineering Centers Building,
1550 Engineering Drive,
Madison, WI 53706
e-mail: philip@surgery.wisc.edu

Shivendra G. Tewari
Molecular & Integrative Physiology,
University of Michigan—Ann Arbor,
2800 Plymouth Road,
North Campus Research Center,
Ann Arbor, MI 48109-5622
e-mail: tewarisg@gmail.com

Claire S. Chen
Mechanical Engineering,
University of Wisconsin—Madison,
2145 Engineering Centers Building,
1550 Engineering Drive,
Madison, WI 53706
e-mail: cchen394@wisc.edu

Mark S. Nyaeme
Biomedical Engineering,
University of Wisconsin—Madison,
2145 Engineering Centers Building,
1550 Engineering Drive,
Madison, WI 53706
e-mail: mnyaeme@wisc.edu

Zhijie Wang
Mechanical Engineering,
Colorado State University,
1301 Campus Delivery,
Fort Collins, CO 80521
e-mail: Zhijie.Wang@colostate.edu

Diana M. Tabima
Biomedical Engineering,
University of Wisconsin—Madison,
2144 Engineering Centers Building,
1550 Engineering Drive,
Madison, WI 53706
e-mail: dtabimamarti@wisc.edu

Anthony J. Baker
Medicine,
University of California—San Francisco,
4150 Clement St,
San Francisco, CA 94121;
VA Medical Center,
4150 Clement St.,
San Francisco, CA 94121
e-mail: Anthony.baker@ucsf.edu

Multiscale Computational Analysis of Right Ventricular Mechanoenergetics

Right ventricular (RV) failure, which occurs in the setting of pressure overload, is characterized by abnormalities in mechanical and energetic function. The effects of these cell- and tissue-level changes on organ-level RV function are unknown. The primary aim of this study was to investigate the effects of myofiber mechanics and mitochondrial energetics on organ-level RV function in the context of pressure overload using a multiscale model of the cardiovascular system. The model integrates the mitochondria-generated metabolite concentrations that drive intracellular actin-myosin cross-bridging and extracellular myocardial tissue mechanics in a biventricular heart model coupled with simple lumped parameter circulations. Three types of pressure overload were simulated and compared to experimental results. The computational model was able to capture a wide range of cardiovascular physiology and pathophysiology from mild RV dysfunction to RV failure. Our results confirm that, in response to pressure overload alone, the RV is able to maintain cardiac output (CO) and predict that alterations in either RV active myofiber mechanics or RV metabolite concentrations are necessary to decrease CO.
[DOI: 10.1115/1.4040044]

[1]Corresponding author.
Manuscript received December 1, 2017; final manuscript received April 13, 2018; published online May 24, 2018. Assoc. Editor: Rouzbeh Amini.

Daniel A. Beard
Molecular & Integrative Physiology,
University of Michigan—Ann Arbor,
2800 Plymouth Road,
North Campus Research Center,
Ann Arbor, MI 48109-5622
e-mail: beardda@med.umich.edu

Naomi C. Chesler[1]
Fellow ASME
Biomedical Engineering,
University of Wisconsin—Madison Medicine,
2146 Engineering Centers Building,
1550 Engineering Drive,
Madison, WI 53706
e-mail: naomi.chesler@wisc.edu

Introduction

Heart failure (HF) is a major cause of morbidity and mortality, with approximately 10% of people over the age of 65 suffering from heart failure in the U.S. [1]. While right ventricular failure (RVF) patients have significantly increased mortality rates compared to left ventricular failure (LVF) patients [2], the majority of heart failure literature focuses on the left ventricle (LV). The RV, however, is anatomically, functionally, and embryologically different from the LV; and RVF has a pathology distinct from LVF [3]. RVF typically occurs in the setting of pressure overload, i.e., pulmonary hypertension (PH), which can occur due to pulmonary arterial disease, left heart disease (LHD), lung disease, thromboembolism, or a combination of these factors. As RVF is the leading cause of death in all-cause PH [4,5], and decreased RV ejection fraction (EF) is a significant risk factor in LVF [2], a better understanding of RV function and failure is key to treatment and management of both PH and LVF patients.

The interactions of cell-, tissue- and organ-level function are critical determinants of RV function. At the cellular level, RV contraction is initiated by the release of Ca^{2+} into the cytosol by the sarcoplasmic reticulum (Fig. 1). Ca^{2+} then binds to troponin C, causing a conformational change that enables actin and myosin cross-bridge reactions [7]. Cross-bridge reactions also depend on mitochondrial adenosine triphosphate (ATP) production and the oxidation of ATP to adenosine triphosphate (ATP) and inorganic

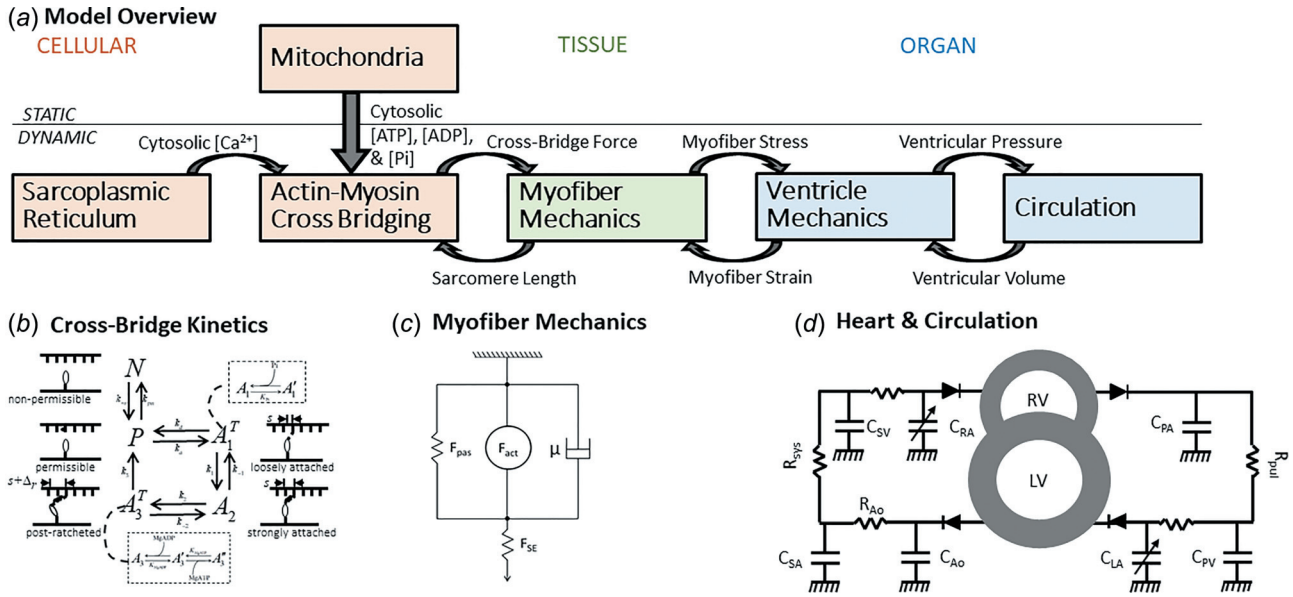

Fig. 1 Schematic of mechanoenergetic computational model of the cardiovascular system adapted from Tewari et al. [6]. (*a*) Overall scheme. At the cellular level, release of calcium from the sarcoplasmic reticulum and metabolites ATP, ADP, and inorganic phosphates (Pi) drives *actin-myosin cross-bridge kinetics*, which drives myofiber mechanics dependent on sarcomere length. At the tissue level, *myofiber mechanics* that incorporate cross-bridge cycling, intracellular titin, and extracellular collagen and generate myofiber stress dependent on myofiber strain. At the organ level, *ventricle mechanics* and intraventricular interactions drive ventricular pressures dependent on ventricular volumes; the *circulation* provides ventricular afterload and the hemodynamic connection between the chambers. (*b*) Diagram of actin-myosin cross-bridging kinetics. Kinetic rates are functions of Ca^{2+} and metabolite concentrations. (*c*) Diagram of myofiber mechanics; F_{pas}: passive force, including contributions of titin and collagen, F_{act}: active force of actin-myosin cross-bridging, μ: viscous force, and F_{SE}: corrective factor for sarcomere length. (*d*) Diagram of heart and circulation; C: compliance, R: Resistance, PA: pulmonary artery, PV: pulmonary veins, SV: systemic veins, Ao: aorta, sys: systemic vasculature, pul: pulmonary vasculature, RA: right atria, RV: right ventricle, LA: left atria, and LV: left ventricle.

phosphates [8]. Contraction of individual sarcomeres within a myocyte, driven by cross-bridge reactions, must overcome passive forces generated by intracellular titin; relaxation of sarcomeres must overcome passive forces generated by both intracellular titin and extracellular collagen [9]. At the tissue level, multiple myocytes surrounded by collagen form a myofiber. The number and the size of myofibers largely determine ventricular wall size and contractility [9]. Ventricular contraction itself depends on its intrinsic contractility as well as extrinsic factors including filling volumes and the downstream circulation [10]. For the RV, contraction also depends on co-contraction of the LV and dynamics of the intraventricular septum [11].

As shown in animal models, at the cell-level, RVF is characterized by decreases in mitochondrial content [12,13] with subsequent changes in ATP metabolites [14] and decreases in maximum Ca^{2+} activated myofilament force (F_{max}) [15,16]. At the tissue-level, RVF often associates with increased passive myocyte stiffness [17,18] and increased interstitial collagen content [19–21]. At the organ-level, RVF is characterized by reduced cardiac output (CO) and reduced RV EF [19–21]. In addition to CO and EF, hemodynamic uncoupling between the ventricle and the vasculature has also been found to predict outcomes of disease [22]. *How changes at the cell- and tissue-level contribute to RVF at the organ-level is a critical knowledge gap.*

Computational models offer a framework for bridging the knowledge gap between cell-, tissue-, and organ-level function. Models of mitochondrial ATP synthesis have proven useful in studying cardiac energetics and ischemia [23,24]. Similarly, simulation of myofiber contraction driven by cross-bridge cycling has been performed [25], with some studies incorporating cooperative myocyte activation [26] and the thermodynamics of metabolite consumption [27]. Connecting cell- and tissue-level function to organ-level function has remained a challenge. Recently, Tewari et al. [6] coupled a cell-level cardiomyocyte model accounting for excitation–contraction coupling, cross-bridge mechanics, and metabolite concentrations [28] to a biventricular cardiac mechanics model developed by Lumens et al. [29]. Briefly, a system of partial differential equations describes the metabolite-dependent chemical kinetics of ATP hydrolysis that drive actin–myosin interaction, which in turn drive active tension developed by cross-bridges kinetics; myofiber mechanical function is described by incorporating the active force generated by cross-bridges with passive forces of titin and collagen; and these myofiber forces drive contraction and relaxation in the RV wall, LV wall, and the interventricular septum [29]. Biventricular contraction and relaxation drive changes in ventricular volumes that are dependent on pressures, which in turn are modulated by simple lumped parameter models representing the resistances and compliances of the systemic and pulmonary circulations. Tewari et al. used this model to predict that changes in LV metabolite pools measured in animal models of LV failure [14] directly contribute to LV systolic dysfunction [6].

Here, we use the Tewari et al. model [6] to explore RVF and analyze the effects of cell- and tissue-level changes on organ-level RV function. Specifically, we investigate the interdependent effects of pathological changes of key features that have been identified in RVF: changes in RV energetics and active and passive RV myofiber mechanics. As in Tewari et al., energetic state is represented by metabolite concentrations [6]. Active myofiber mechanics are represented by F_{max}; passive myofiber mechanics are represented by contributions of intracellular titin and extracellular collagen, parameters present in the original Tewari paper but whose effects were not studied.

We considered three distinct murine models of RV disease: (1) an angioproliferative form of PH that led to RV dysfunction (decreased EF and ventricular-vascular uncoupling) but not failure (i.e., CO was maintained) and had preserved F_{max} [18]; (2) PH due to interstitial pulmonary fibrosis in which decreases in CO and EF as well as F_{max} was found [15]; and (3) PH secondary to LHD which leads to maintained CO 16 weeks after disease onset [30] and maintained F_{max} at 12 weeks after disease onset [15,16]. Based on the first two disease models, we hypothesize that changes in F_{max} will have the greatest effect on the ability of the RV to maintain CO. We considered the third case to explore the ability of the model to predict the dependence of RV function on LV function.

Methods

This section details the framework of the cardiovascular mechanoenergetic model, the experimental small animal models of disease, our approach to simulating pathologies, and the protocol for parameter studies to further explore the effects of metabolite concentrations, F_{max}, and RV myofiber mechanics.

Mechanoenergetic Model of Cell and Tissue Level Function. The modeling framework developed by Tewari et al. [6] incorporates a biventricular heart model [29] to describe realistic ventricular mechanics and couples this with a lumped parameter circulation (Fig. 1). Models of myocyte cross-bridge cycling and force generation [28] drive contraction and relaxation in the RV free wall, LV free wall, and septum. As shown in Fig. 1, static (i.e., constant) metabolite concentrations and dynamic (i.e., transient) cytosolic Ca^{2+} concentration drive actin-myosin cross-bridging. Cross-bridge force is used with a sliding-filament sarcomere in the myofiber tissue model to determine myofiber stress. Myofiber stress is used to calculate ventricular pressures, and ventricular pressures drive flow in the lumped parameter circulation. Circulatory flows cause changes in ventricular volume, myofiber strain, and sarcomere length, affecting ventricular pressure, myofiber stress, and cross-bridge force, respectively. Additional model details are presented in the Appendix.

Organ Level Right Ventricular Function. Metrics of RV function include EF, RV end-systolic pressure (P_{ES}), arterial elastance (E_a), end systolic elastance (E_{es}), ventricular-vascular coupling (VVC), and CO. The calculations of EF, E_a, and VVC from simulated ventricular pressures and volumes are shown in Eqs. (3)–(5) [10], where V_{ES} is the end-systolic volume and V_{ED} is the end-diastolic volume. The gold standard method for computing end systolic elastance (E_{es}) is the slope of the line connecting end systolic points in the pressure-volume plane from several heartbeats at varied preload [10]. Because multiple heartbeats with varied preload are not simulated, we use a single-beat approximation to VVC based on volumes [22], which is known to underestimate VVC [10]

$$\mathrm{EF} = \frac{V_{ED} - V_{ES}}{V_{ED}} \tag{1}$$

$$E_a = \frac{P_{ES}}{V_{ED} - V_{ES}} \tag{2}$$

$$\mathrm{VVC} = \frac{E_{es}}{E_a} \cong \frac{V_{ED} - V_{ES}}{V_{ED}} \tag{3}$$

Parameter Estimation

Vascular Resistance and Compliance Estimation. Pulmonary vascular resistance (PVR) was assumed proportional to the total pulmonary vascular resistance, which does not incorporate left atrial pressure, and was calculated from experimental data as

$$\mathrm{PVR} = \frac{P_{ES}}{\mathrm{CO}} \tag{4}$$

Pulmonary arterial compliance (C_{PA}) values were calculated from experimental data as

$$C_{PA} = \frac{SV}{PP_{PA}} \tag{5}$$

where SV is the stroke volume and PP_{PA} is the pulmonary artery pulse pressure. If PP_{PA} was not available to directly calculate C_{PA}, C_{PA} was instead decreased from baseline value (see Table 4 for baseline values of all parameters) until simulated E_a matched experimental E_a to within 10%. In simulations of disease, blood volume and systemic vascular resistance were increased to maintain systolic systemic arterial pressures in a normal range (110–125 mmHg) as done previously [6].

Metabolite Concentration Estimation. The cross-bridge model couples energetics with mechanics by explicitly modeling binding/unbinding of ATP, ADP, and inorganic phosphates (Pi) with the actin-myosin complex. Healthy and failure metabolite concentrations were previously calculated [6] based on data from a canine LV hypertrophy model [14].

F_{max} Estimation. The contractile mechanical behavior of a myofiber is described by the active force generated by cross-bridges. Experimentally observed decreases in F_{max} with RVF [15] (Fig. 2) were represented in silico by decreasing the myosin head stiffness ($k_{stiff,2}$ in Eq. (A7)), which is an important contributor to the force-pCa^{2+} relationship from which F_{max} is derived.

Passive Right Ventricular Myofiber Mechanics Estimation. Changes in passive RV myofiber mechanics were assumed to be from contributions of titin intracellularly and collagen extracellularly. The myofiber constitutive relationship parameter representing collagen content ($PCon_{collagen}$) was increased to match fibrosis (i.e., collagen accumulation) if reported experimentally. The constitutive relationship parameter representing titin ($PCon_{titin}$) was increased to match passive force measurements at a sarcomere length of 2.2 μm per the literature [18].

Cardiovascular Disease Models. The three small animal models of RV dysfunction and failure were simulated to explore a range of physiological phenomena and examine mechanisms by which RV pathology may occur. The disease models are categorized as either pulmonary arterial hypertension (PAH), defined as PH with increased PVR and normal left atrial pressure (angioproliferative, caused by exposure to chronic hypoxia and the VEGF receptor inhibitor SUGEN; or interstitial pulmonary fibrosis, caused by exposure to the antibiotic bleomycin), or PH secondary to left heart disease (PH-LHD) (caused by myocardial infarction (MI)). RV function from simulations where metabolite concentrations, F_{max}, or RV myofiber mechanics were altered was compared against experimental measurements of RV hemodynamics and function for each pathology.

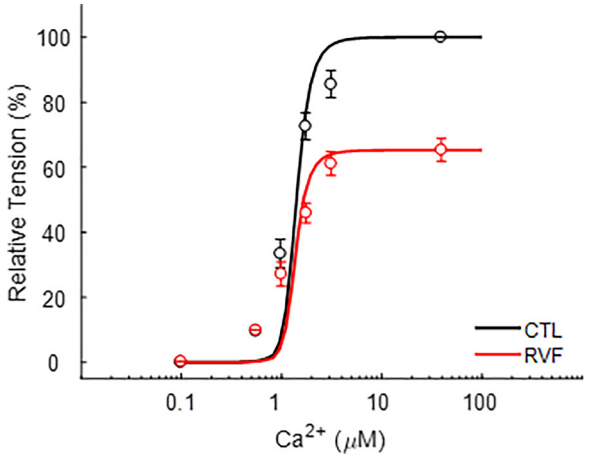

Fig. 2 Good agreement is observed between experimental [15] and simulated myofilament force versus pCa^{2+}, especially at maximum myofilament force

Bleomycin. Bleomycin (Bleo) is a fibrinogenic antibiotic that causes interstitial pulmonary fibrosis followed by PAH and RV failure. Changes in PVR and C_{PA} in bleomycin-treated mice were estimated from Hemnes et al. [31]. Pathological changes in metabolite concentrations, F_{max}, and RV myofiber mechanics were all simulated. Simulation parameters that were varied from baseline in the Bleo simulations are listed in Table 1.

Sugen Hypoxia. Sugen Hypoxia (HySu) exposure in mice leads to PAH and RV ventricular-vascular uncoupling although cardiac output is maintained. HySu PVR and C_{PA} were calculated from hemodynamic measurements [18,32]. Pathological changes in metabolite concentrations, F_{max}, and RV myofiber mechanics were simulated. Simulation parameters that were varied from baseline in the HySu simulations are listed in Table 2.

Left Ventricle Myocardial Infarction. Ligation of the left-anterior-descending coronary artery causes a MI which can result in PH-LHD. To simulate the MI model of PH-LHD, LV wall metabolite concentrations were set to failure values calculated from Ref. [6]. Pathological changes in RV F_{max} and RV metabolite concentrations were simulated. As neither changes in passive myofiber mechanics nor RV fibrosis have been reported in the murine MI model, RV myofiber mechanics were not changed from baseline. Simulation parameters that were varied from baseline in the PH-LHD simulations are listed in Table 3.

Parameter Study. After using the mechanoenergetic model to explore several types of RV disease, we sought answers to two questions raised by our results: (1) What is the relative importance of F_{max} and metabolite concentration on RV function and is this relative importance dependent on afterload? (2) Can the model capture RV diastolic dysfunction due to increased RV myofiber stiffness? To answer these questions, two parameter studies were performed.

Maximum Myofiber Force versus *Metabolite Concentration.* To determine the relative effects of F_{max} and metabolite concentration, five values evenly spaced between healthy and failure values for both F_{max} and metabolite concentrations were used. The resulting 25 combinations of forces and metabolite concentrations were then used in the simulation with PVR set at 1, 2, and 4 times control. The simulated RV EF values were then correlated with both F_{max} and ATP concentration using a linear regression. Summed squared error of the linear regression was used as a metric of correlation strength.

Right Ventricular Myofiber Mechanics. It was surprising that increased passive RV stiffness through titin and/or collagen did not meaningfully affect simulation results in either the Bleo or HySu models. To determine if the model can capture changes in diastolic function that would result from increased RV myofiber stiffness, the passive force contributions from titin and collagen were incrementally increased up to 40 times control values in simulations with no other dysfunction except PVR set at four times control. Passive ventricular stiffness was quantified by fitting an exponential to the diastolic portion of the RV PV loop and calculating the slope at end diastole, which is the end diastole pressure volume relationship (EDPVR)

$$\text{EDPVR} = \left.\frac{\partial P}{\partial V}\right|_{V_{dia}} \tag{6}$$

Cardiac output was used as a metric of overall RV function.

Table 1 Bleo parameters

Parameter	Baseline value	Bleo value	Reference
Pulmonary vasculature			
PVR	19.2 mmHg s mL^{-1}	56.8 mmHg s mL^{-1}	Hemnes et al. [31]
C_{PA}	2.42 mL $mmHg^{-1}$	0.73 mL $mmHg^{-1}$	Hemnes et al. [31]
RV parameters			
$k_{stiff,2}$	51.9 MPa μm^{-1}	33.2 MPa μm^{-1}	Cowley et al. [15]
$PCon_{collagen}$	0.02 (normalized force)	0.054 (normalized force)	Cowley et al. [15]
[ATP]	8.0 mM	1.6 mM	Tewari et al. [6]
[ADP]	18 μM	4 μM	Tewari et al. [6]
[Pi]	0.6 mM	4 mM	Tewari et al. [6]

Table 2 HySu parameters

Parameter	Baseline value	HySu value	Reference
Pulmonary vasculature			
PVR	19.2 mmHg s mL^{-1}	34.4 mmHg s mL^{-1}	Wang et al. [18]
C_{PA}	2.42 mL $mmHg^{-1}$	1.36 mL $mmHg^{-1}$	Liu et al. [12]
RV parameters			
$k_{stiff,2}$	51.9 MPa μm^{-1}	33.2 MPa μm^{-1}	Cowley et al. [15]
$PCon_{collagen}$	0.02 (Normalized force)	0.1446 (Normalized force)	Wang et al. [18]
$PCon_{titin}$	0.002 (Normalized force)	0.003 (Normalized force)	Wang et al. [18]
[ATP]	8.0 mM	1.6 mM	Tewari et al. [6]
[ADP]	18 μM	4 μM	Tewari et al. [6]
[Pi]	0.6 mM	4 mM	Tewari et al. [6]

Table 3 MI parameters

Parameter	Baseline value	MI value	Reference
LV parameters			
[ATP]	8.0 mM	1.6 mM	Tewari et al. [6]
[ADP]	18 μM	4 μM	Tewari et al. [6]
[Pi]	0.6 mM	4 mM	Tewari et al. [6]
RV parameters			
$k_{stiff,2}$	51.9 MPa μm^{-1}	33.2 MPa μm^{-1}	Cowley et al. [15]
[ATP]	8.0 mM	1.6 mM	Tewari et al. [6]
[ADP]	18 μM	4 μM	Tewari et al. [6]
[Pi]	0.6 mM	4 mM	Tewari et al. [6]

Results

Cardiovascular Disease Models

Bleomycin. The effects of altered cell-level metabolite concentrations and increased tissue-level RV myofiber stiffening and maximum force were explored in the Bleo model of PAH. Initially, Bleo exposure was simulated by increasing PVR from hemodynamic measurements and decreasing pulmonary artery compliance to match RV E_a from Ref. [31] (Fig. 3(*a*)). Using baseline RV parameters, E_{es} was maintained, VVC decreased (Figs. 3(*b*) and 3(*c*)), RV systolic pressure (RVSP) increased (Fig. 3(*d*)), and CO decreased minimally (Fig. 3(*e*)). Increasing the RV collagen content had negligible effects on these parameters.

Heart failure-like changes in either metabolite concentration or F_{max} led to a decrease in E_{es} (Fig. 3(*b*)), which consequently decreased CO and therefore led to better agreement with the experimentally observed decrease in CO; however, the changes in RVSP and EF underpredicted measured changes (Figs. 3(*d*)–3(*f*)). The degree of RV dysfunction caused by HF metabolite concentrations and decreased F_{max} was similar.

In summary, the multiscale model predicted RV failure in response to pressure overload, as evidenced by a high degree of ventricular-vascular uncoupling and decreased CO, similar to experimental results only when RV mechanoenergetics were altered in addition to RV afterload.

Sugen Hypoxia. The effects of altered cell-level metabolite concentrations and increased tissue-level RV myofiber stiffening and maximum force also were explored in the HySu model of PAH, which led to a less severe pressure overload than Bleo. The effect of HySu on RV afterload was simulated by increasing PVR and decreasing C_{PA}, as shown in Fig. 4(*a*). Simulations with PH and PH plus increased RV myofiber stiffness, from both titin and collagen, match the experimental data well (Figs. 4(*b*)–4(*f*)). As in the Bleo simulations, little difference is observed between simulated PH and simulated PH with increased RV myofiber stiffness (Figs. 4(*a*)–4(*f*)). The model accurately predicts this mild form of PH and RV dysfunction, with decreases in EF and VVC and maintained CO.

Simulating HySu-induced PH with HF metabolite concentrations and decreased F_{max}, respectively, predicts a decrease in CO not observed experimentally, and overpredicts decreases in RV EF, E_{es}, and VVC (Figs. 4(*b*)–4(*f*)). Unlike the Bleo simulations, in which decreased F_{max} and HF metabolite concentrations had similar effects on these parameters, in the HySu simulations, decreasing F_{max} caused slightly more RV dysfunction than simulations with HF metabolite concentrations.

Left Ventricle Myocardial Infarction. The effects of altered cell-level metabolite concentrations and decreased tissue-level RV maximum force were explored in the MI model of PH-LHD. Initially, PH-LHD was simulated with HF metabolite concentrations in the LV wall. This change had little effect on LVSP (Fig. 5(*a*)) and decreased LV EF (Fig. 5(*b*)). LV EDP did increase, but less than reported experimentally (Fig. 5(*c*)). Typical of secondary PH, predicted RV E_a increased (Fig. 5(*d*)). These LV changes did not alter predicted RV E_{es}, but imposing HF metabolite concentrations in the RV and decreasing F_{max} in the RV free wall did predict decreased E_{es} (Fig. 5(*e*)). VVC was predicted to decrease with PH-LHD and then decrease further with HF metabolite concentrations and decreased F_{max} in the RV (Fig. 5(*f*)). As in experiments, simulated CO was maintained (Fig. 5(*h*)) and RV EF was predicted to decrease (Fig. 5(*i*)).

In summary, the mechanoenergetic model predicted an MI phenotype: increased LV EDP leading to increased E_a and RVSP. Decreasing RV maximum force or altering metabolites further decreased E_{es}, which in turn decreased VVC.

Parameter Study

Maximum Myofilament Force Versus Metabolite Concentration. The RV EF from simulations comparing F_{max} and metabolite concentrations are shown in Fig. 6. At all simulated levels of PVR, decreases in F_{max} or metabolic dysfunction cause decreased RV EF. Interestingly, the predicted relative effects of F_{max} and metabolite concentration depend on afterload. At control PVR (Figs. 6(*a*) and 6(*b*)), F_{max} has a much stronger correlation with RV EF than metabolite concentration. At a two times increase in PVR (Figs. 6(*c*) and 6(*d*)), F_{max} still exhibits a stronger correlation with RV EF than metabolite concentration. However, at a four times increase in PVR (Figs. 6(*e*) and 6(*f*)), F_{max} and metabolite concentration have similar correlations with RV EF and, in fact, metabolite concentration has a marginally lower summed-squared-error.

Passive Right Ventricular Myofiber Mechanics. With increased PVR, the ventricle dilates (Fig. 7(*a*)). This dilation causes an increase in EDPVR (Fig. 7(*b*)). With ventricle dilation, sarcomeres in the RV wall are elongated beyond 2.25 μm (Fig. 7(*e*)), which is the length at which collagen is loaded in the myofiber constitutive model [26]. RV wall passive stress is thus increased compared to control (Fig. 7(*f*)). In simulations at four times increase in PVR, increasing RV myofiber stiffness decreases CO as well as EDPVR (Figs. 7(*c*) and 7(*d*)). With increased RV myofiber stiffness, RV wall passive stress increases (Fig. 7(*f*)). The stiff RV myofiber and subsequent passive stresses act as a penalty to loading collagen, which can be seen in Fig. 7(*e*), where the RV tissue is only briefly stretched to the point of collagen loading. The inability of RV tissue to stretch, and thus the RV to fill, likely decreases CO. Thus, the absence of RV free wall collagen loading due to increased RV myofiber stiffness decreases the EDPVR.

Discussion

Multiscale computational models have become an increasingly popular tool to study the cardiovascular system as they enable the effects of cell and tissue level phenomena on organ level function to be quantified [34]. These models have been developed in areas such as mechanoenergetics [6], electromechanical coupling [35], and growth and remodeling [36]. Multiscale models also provide insight into pathophysiology not available through experimental means, and with increased validation, may help identify and design novel therapies.

In this study, a multiscale model of cardiovascular mechanoenergetics was used to simulate three types of RV disease: PAH with maintained CO, PAH with decreased CO, and PH secondary to left heart disease. In the latter case, the LV contribution to RV ejection is impaired and thus represents a good test of the model's ability to simulate biventricular function. While the accuracy of the mechanoenergetic, biventricular model to simulate subject specific outcomes remains unknown, this study demonstrated reasonable agreement with population-average experimental results from three types of RV disease, a promising step toward validation of this model. Moreover, key findings include the following:

(1) Maximum calcium-activated force and metabolic energetic state have a strong and direct effect on organ-level RV function in simulations, confirming experimental correlations between cell and organ function;
(2) organ-level changes in biventricular mechanics, such as increased RV chamber volume due to pressure overload or impaired LV pumping due to MI, affect RV cell- and tissue-level function, also confirming experimental physiological data; and
(3) F_{max} has a greater impact on organ-level RV function than metabolite concentration at mild pressure overload, but a similar impact on organ-level RV function at a more severe pressure overload, a novel observation derived from our study that can be tested in future experiments.

Energetics. The previous studies have shown that mitochondria function is impaired in RVF and RV dysfunction [12,13]. Prior work with this mechanoenergetic model has shown that changing LV metabolite concentration with no other vascular or ventricular changes causes LV failure [6]. Simulations in this study predict that in the setting of increased RV afterload, metabolic changes in the RV decrease CO, EF, and E_{es}. In contrast, only EF is decreased by increased afterload alone.

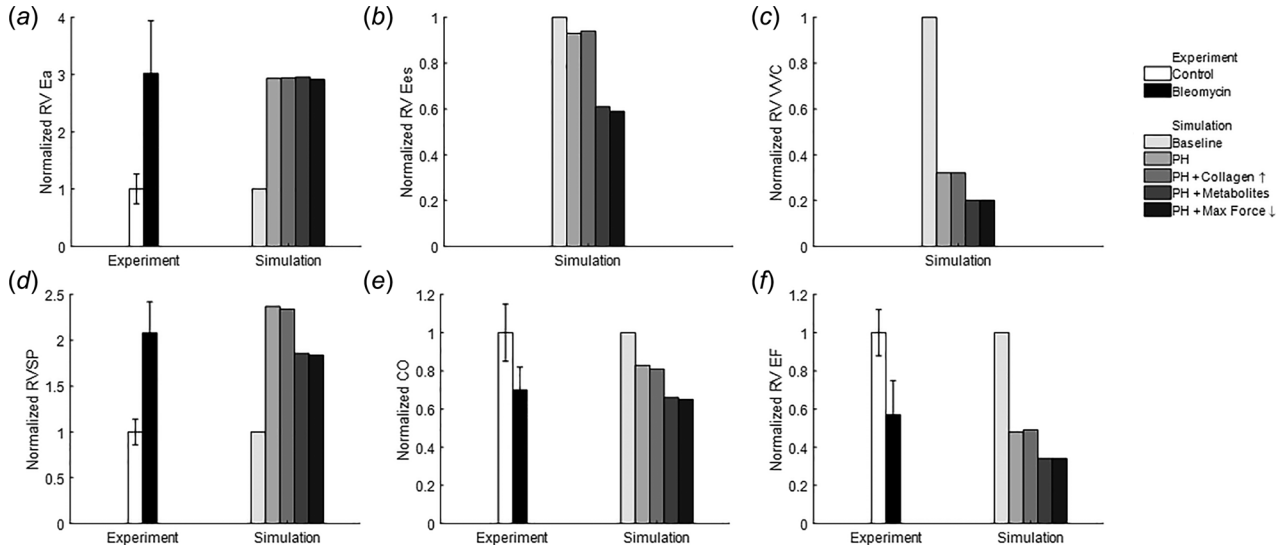

Fig. 3 Comparison of Bleo experimental [31] and simulated PH. Error bars represent interquartile range. ((*a*)–(*c*)) Simulation predicts preserved E_{es} until metabolites or maximum force changes, and that maximum force and metabolite changes result in further VVC decreases compared to PH alone. ((*d*)–(*f*)) PH alone and PH + increased RV stiffness overestimate RVSP and CO but match EF, while changing maximum force and metabolites matches CO but underestimates RVSP and EF.

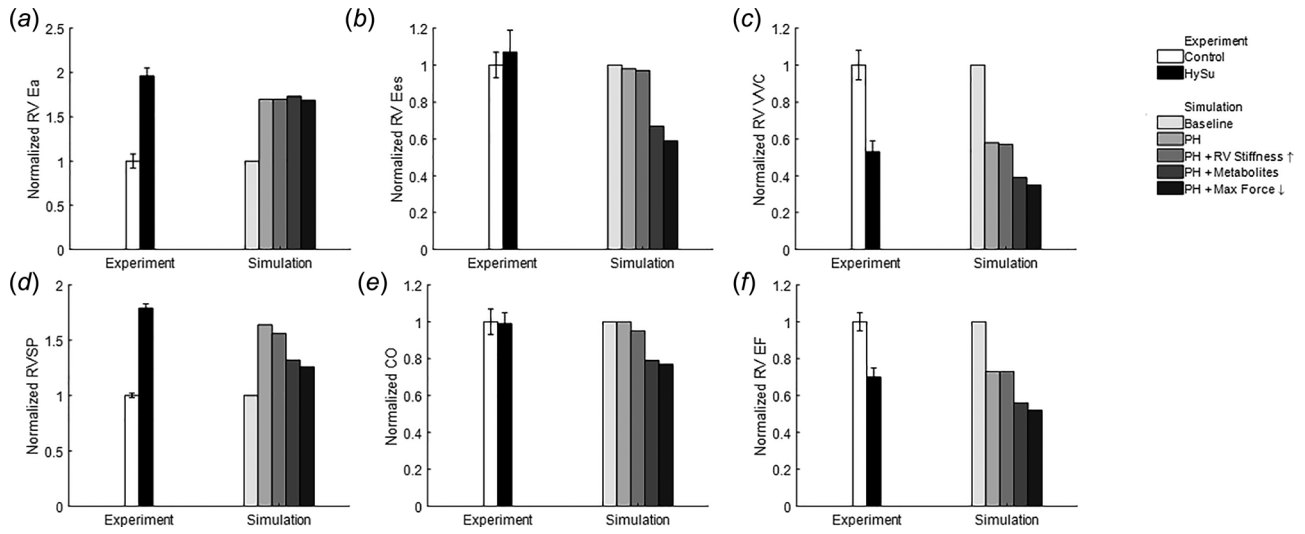

Fig. 4 Comparison of HySu experimental [16] and simulated PH. Error bars represent standard error. PH alone and PH + increased RV stiffness match all hemodynamic parameters well, but changing metabolite concentration and maximum force causes more severe decreases in RV function than observed experimentally.

Active Mechanics. Experimental models of PH have shown decreased F_{max} with decreased cardiac output [15], and conversely maintained F_{max} has been observed with preserved cardiac output [18]. Our simulations suggest a causal relationship between maximum myofilament force and cardiac output. In the HySu and MI models, CO is initially maintained and then decreases when the maximum myofilament force is decreased (Figs. 5 and 6). Similarly, in the Bleo model, decreasing maximum myofilament force decreases CO much more than increases in RV afterload alone (Fig. 4).

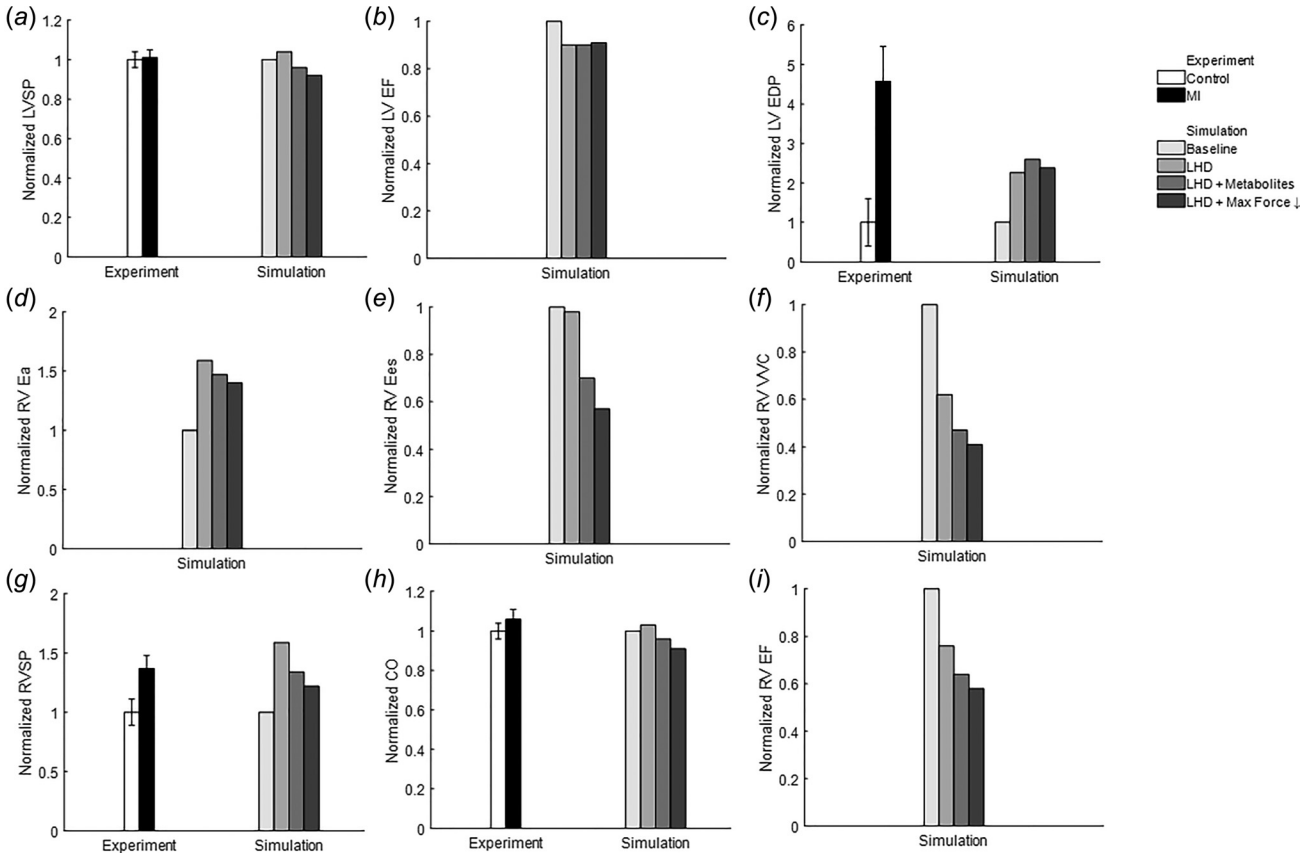

Fig. 5 Comparison of MI experimental [30,33] and simulated PH-LHD. Error bars represent standard error. (*a*) LVSP is maintained in both experiments [30] and simulation. (*b*) LV EF is predicted to decrease slightly with LHD (HF metabolites in the LV). (*c*) LV EDP increase is not as severe in simulation as experiment [33]. (*d*) Simulations predict increased RV afterload, (*e*) while changing RV metabolites or myofilament force is necessary to decrease Ees, thus (*f*) VVC is predicted to decrease with LHD, and further decrease with impaired RV cellular function. (*g*) LHD alone overestimates RVSP, while changing myofilament force and metabolites slightly underestimates RVSP [30]. (*h*) CO is maintained both experimentally [30] and in simulation. (*i*) Simulations predict decreased RV EF.

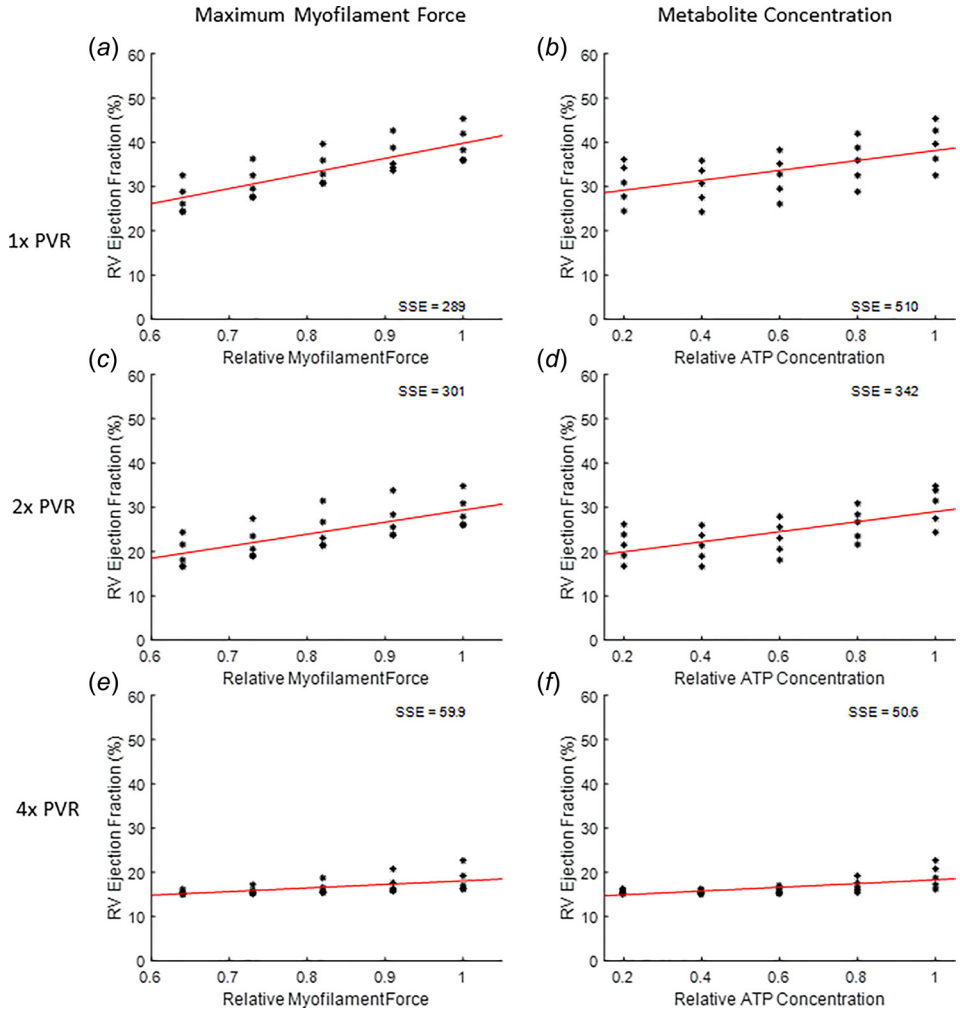

Fig. 6 Parameter study correlating RV EF with myofilament force and metabolite concentration. (*a*) At 1x PVR, maximum myofilament force has a much stronger correlation with EF than (*b*) metabolite concentration has with EF. (*c*) At 2× PVR, maximum myofilament force still exhibits a stronger correlation with EF than (*d*) the correlation between metabolite concentration and EF. E. At 4× PVR, maximum myofilament force exhibits a similar correlation with EF as (*f*) the correlation between metabolite concentration and EF.

Mechanoenergetic Interactions. Interestingly, the relative importance of F_{max} and metabolite concentration on RV function was found to be RV afterload dependent. In simulations of mild pressure overload (HySu and MI), F_{max} has a greater effect on RV function than metabolite concentration (Figs. 5 and 6), but in severe pressure overload (Bleo), F_{max} and metabolite concentration have similar effects (Fig. 4). The parameter study comparing F_{max} and metabolite concentration confirms this relationship. At control PVR values, the maximum myofilament force has a much stronger correlation with RV EF than metabolite concentration, while at a four times increase in PVR, the correlations are nearly the same. The simulation findings that at lower afterloads myofilament force changes have a greater effect than energetic changes are supported by experimental evidence. In mild pressure overload in mice, mitochondrial dysfunction has been observed, but CO is maintained [12,13], suggesting that the mitochondrial dysfunction has minimal effects. Mild and severe pressure overload exhibit a similar degree of mitochondrial dysfunction [13] but only in severe PH do markers of mitochondrial function correlate with RV function [13]. These simulation findings have a potential impact on RV disease treatment strategy as only active myofiber mechanics would need to be treated to rescue RV function in a patient with mild pressure overload, whereas in a patient with severe pressure overload both active myofiber mechanics and mitochondria function should be RV treatment targets.

Passive Mechanics. Right ventricular fibrosis has been widely observed in RV disease [17,19,20,37,38] and is believed to contribute to diastolic dysfunction. Increased myocyte passive stiffness has also been observed [18]. Simulations showed that increased RV myofiber stiffness from both collagen and titin contributions has negligible effects on RV function (Figs. 4 and 5). Simulations do show increased EDPVR due to collagen recruitment as the RV dilates (Fig. 7), so the model is capable of simulating diastolic dysfunction. In the parameter study of RV myofiber stiffness, decreased CO was observed, but only at stiffness increases much higher than have been reported experimentally. Unexpectedly, EDPVR decreased in simulations with increased RV stiffness. Figure 7(*f*) illustrates that with 40× increased RV stiffness, RV wall passive stresses are nearly an order of magnitude greater than baseline. These increases in

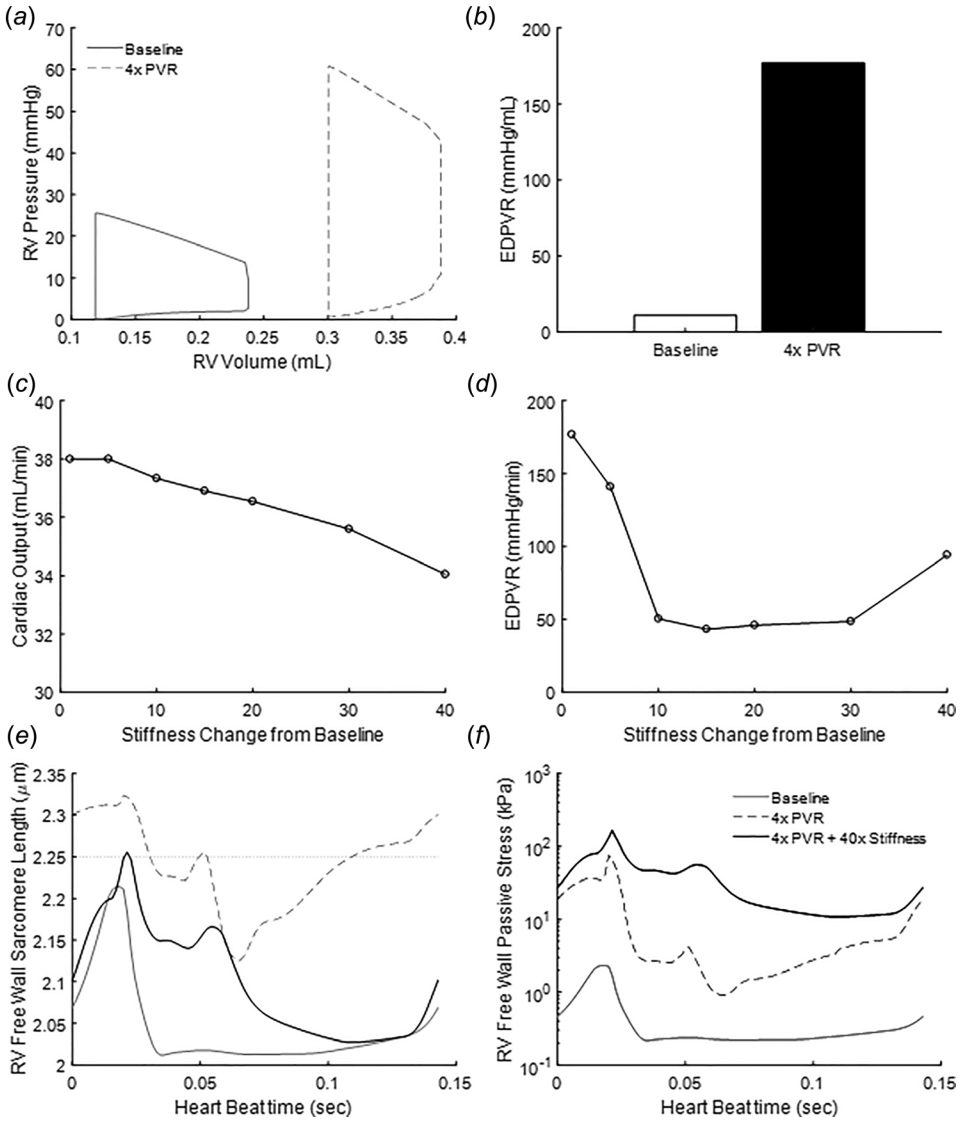

Fig. 7 EDPVR increases with RV dilation and increased RV stiffness decreases CO but not EDPVR. (*a*) Pressure overload increases RV end diastolic volume, (*b*) which results in increased EDPVR, (*c*) increasing RV stiffness decreases CO, (*d*) but instead of increasing EDPVR, increased RV stiffness decreases EDPVR. (*e*) With increased afterload, RV sarcomeres are elongated, and increased stiffness prevents this elongation. (*f*) With increased afterload, RV passive stress increases, and increasing RV stiffness further increases RV passive stress.

passive stress prevent sarcomere elongation to the point where collagen is loaded (Fig. 7(*e*)). This could explain decreased EDPVR, as with increased RV myofiber stiffness the ventricle is not dilated to the point where collagen is loaded. Costandi et al. have also shown that increased ventricular compliance can occur with stiffer myocardial material properties [39], although their finite element model included changes in unloaded ventricle volume that we did not consider.

In this model, increased RV myofiber stiffness prevents RV dilation, resulting in decreased CO. Whether or not this simulated behavior represents RV physiology is unclear, as in vivo other parameters (e.g., RV anatomy, strength of atrial contraction) may be changing in tandem with RV myofiber stiffness to affect diastolic function. It is important to note that assumptions about axisymmetric ventricular anatomy and uniaxial mechanical loading in the biventricular heart model may limit the model's sensitivity to changes in RV myofiber mechanics. RVF passive mechanics are more nuanced than changes in stiffness as RV wall myocyte and collagen fiber orientations are altered in response to pressure overload [40], and recent work by Avazmohammadi et al. suggests that myofibril–collagen interactions may play an important role in passive RV mechanics [41].

Limitations. Limitations of this study at the cellular level include that failure metabolite concentrations determined from an LV failure model might not be accurate for RV metabolite concentrations in failure. Given the results of the parameter study (Fig. 6), we expect that changes in metabolite concentrations would still impair RV function compared to pressure overload alone. A second energetic limitation of this model is that the metabolism-dependence of sarcoplasmic endoplasmic reticulum Ca^{2+} ATPase (SERCA) is not represented. As limited effects were seen from increased RV myofiber stiffness, it is unclear if increased diastolic Ca^{2+} concentrations would disrupt diastolic function in this model. In our analysis, it was assumed that

decreases in F_{max} were due to the myofilament head stiffness ($k_{stiff,2}$ in Eq. (A7)), but theoretically changes in actin-myosin kinetic rates would also decrease F_{max} (Eq. (A12)) in addition to affecting rate of force development, which the myofilament head stiffness does not. Finally, only intrinsic material properties were explored in this study, so changes in RV anatomy at the organ level such as concentric and eccentric hypertrophy were not considered. As RVSP was underestimated in the HySu simulations and the Bleo and MI simulations with failure force or metabolites, RV hypertrophy as an adaptive response could be incorporated in future work.

Conclusion

This study used a multiscale model of the cardiovascular system to quantify the effects of metabolite concentrations as well as active and passive cardiac tissue mechanics on RV function. Simulations predict that maximum myofilament force and metabolite concentrations strongly control RV function and CO. Additionally, simulations predict the relative importance of maximum myofilament force and metabolite concentrations which is dependent on the degree of RV pressure overload. Overall, this study shows that while further validation is needed in the area of diastolic RV function, the multiscale mechanoenergetic model is a useful tool to explore mechanisms of RV systolic dysfunction and failure.

Funding Data

- National Heart, Lung, and Blood Institute Grant R01 HL-086939 (N.C.C., R.J.P and D.M.T.).
- The Grainger Foundation Wisconsin Distinguished Graduate Fellowship (R.J.P.).
- The Thoracic Surgery Foundation for Research and Education Nina Starr Braunwald Fellowship (J.L.P.).
- Department of Veterans Affairs Merit Review Award I01BX000740 (A.J.B).
- The American Heart Association Grant in Aid 15GRNT25550041 (A.J.B).
- NIH R01 HL-072011 (D.A.B).

Nomenclature

C_{PA} = pulmonary artery compliance
CO = cardiac output
E_a = arterial elastance
E_{es} = end systolic elastance
EDPVR = end diastolic pressure volume relationship
EF = ejection fraction
HF = heart failure
LV = left ventricle
LVF = left ventricular failure
PAH = pulmonary arterial hypertension
PH = pulmonary hypertension
PH-LHD = pulmonary hypertension with left heart disease
PVR = pulmonary vascular resistance
RV = right ventricle
RVF = right ventricular failure
V_{Dia} = end diastolic volume
V_{Sys} = end systolic volume
VVC = ventricular-vascular coupling

Appendix

The mechanoenergetic model was developed by Tewari et al. [6], based on prior validated models of myocardial metabolism [24,42,43], cardiac cross-bridge dynamics [28], and ventricular mechanics [29]. The myocyte energetic state affects cross-bridge cycling and thus myofilament force generation. Active myofilament force generation is coupled to passive forces contributed by titin intracellularly and collagen extracellularly and represented as myofiber mechanics. These myofiber mechanics drive a three-segment model of biventricular mechanics that is integrated with lumped parameter circulations to simulate whole body hemodynamics.

The different scales considered in this model are directly coupled through their governing equations (Fig. 8), resulting in a system of ODEs that can be written as

$$\frac{dX_i}{dt} = f(X_i, t) \tag{A1}$$

where X_i represents system variables ranging in scale from actin-myosin cross-bridging states to circulatory compartment volumes. The ODE system represented in Eq. (A1) is then solved numerically, with all the scales in the model updated every time point.

Cross-Bridge Kinetics. The cross-bridge model couples energetics with mechanics by explicitly modeling binding/unbinding of ATP, ADP, and Pi with actin-myosin complex. Tewari et al. [28] reduced their detailed nine-state model to a five-state model by assuming rapid binding/unbinding ATP, ADP, and Pi. The five state cross-bridge model is shown in Fig. 1. State probabilities are denoted $N(t)$, $P(t)$, $p_1(t,s)$, $p_2(t,s)$, and $p_3(t,s)$, where t is the time and s is the strain. N is a nonpermissible state, P is permissible, and p_1, p_2 and p_3 are the three attached states. These state variables obey conservation according to

$$N(t) + P(t) + \int_{-\infty}^{\infty} p_1(t,s)ds + \int_{-\infty}^{\infty} p_2(t,s)ds + \int_{-\infty}^{\infty} p_3(t,s)ds = 1 \tag{A2}$$

Ca^{2+} release from the sarcoplasmic reticulum (SR) regulates the transition between the nonpermissible and permissible states. SR behavior is not modeled, instead a representative cytosolic Ca^{2+} concentration transient is provided to drive the nonpermissible to the permissible transition. The PDEs controlling cross-bridge kinetics can be reduced to ODEs by expressing the PDEs in terms of the state variable moments [44] and was done in

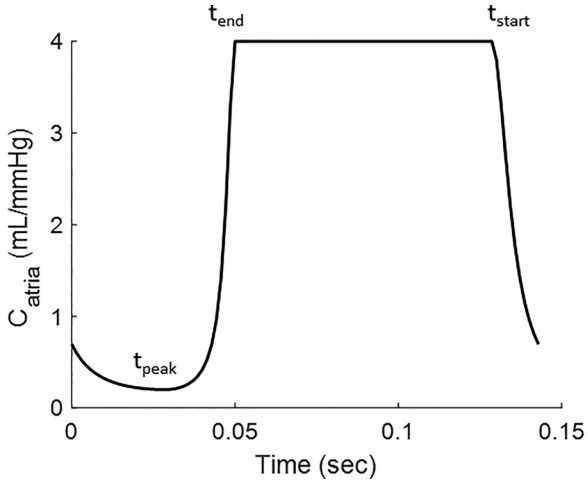

Fig. 8 Plot of time varying atrial compliance. When compliance is low, the atrium is contracting, and when compliance is high, the atrium is relaxed.

Ref. [28]. Using the first three order moments, 1.5% error was found previously between the ODE approximation and the full PDE [28].

Myofiber Mechanics Model. The sarcomere model of Tewari et al. [6] is formulated as follows. The myosin-actin overlap is

$$\begin{aligned} \mathrm{OV}_{z-\mathrm{axis}} &= \min\left(\frac{L_{\mathrm{thick}}}{2}, \frac{\mathrm{SL}}{2}\right), \\ \mathrm{OV}_{M-\mathrm{line}} &= \max\left(\frac{\mathrm{SL}}{2} - (\mathrm{SL} - L_{\mathrm{thin}}), \frac{L_{\mathrm{bare}}}{2}\right) \\ \mathrm{LOV} &= \mathrm{OV}_{z-\mathrm{axis}} - \mathrm{OV}_{M-\mathrm{line}} \end{aligned} \tag{A3}$$

where $\mathrm{OV}_{\mathrm{z\text{-}axis}}$ and $\mathrm{OV}_{\mathrm{M\text{-}line}}$ is the Z region and M-line overlap, respectively. L_{thick} and L_{thin} are the thick and thin filament lengths, respectively. SL is the sarcomere length and L_{bare} is the unbound length of the thick filament. The length of overlap (LOV) is then used to calculate the actin-myosin filament overlap

$$\mathrm{OV}_{\mathrm{thick}} = \frac{2\mathrm{LOV}}{L_{\mathrm{thick}} - L_{\mathrm{bare}}}, \quad \mathrm{OV}_{\mathrm{thin}} = \frac{\mathrm{LOV}}{L_{\mathrm{thin}}} \tag{A4}$$

The transition from nonpermissible (N) to permissible (P) binding is affected by actin overlap fraction ($\mathrm{OV}_{\mathrm{thin}}$) as $\mathrm{OV}_{\mathrm{thin}}$ alters the Ca^{2+}-Troponin C (TrpC) binding affinity

$$\mathrm{TrpReg} = (1 - \mathrm{OV}_{\mathrm{thin}})\mathrm{CaL} + \mathrm{OV}_{\mathrm{thin}}\mathrm{CaH}$$

$$\beta_{\mathrm{NtoP}} = \left(\frac{1}{\left(\frac{\beta_{50}}{\mathrm{TrpReg}}\right)^{n\beta} + 1}\right)^{\frac{1}{2}} \tag{A5}$$

$$\beta_{\mathrm{PtoN}} = \min\left(100, \frac{1}{\beta_{\mathrm{NtoP}}}\right)$$

β_{NtoP} and β_{PtoN} enable the nonpermissible to permissible transition rate to be functions of both Ca^{2+} and $\mathrm{OV}_{\mathrm{thin}}$

$$\begin{aligned} k_{\mathrm{NtoP}}^{\mathrm{App}} &= k_{\mathrm{NtoP}}\beta_{\mathrm{NtoP}}Q_{k_{\mathrm{NtoP}}}^{\frac{T-37.5}{10}} \\ k_{\mathrm{PtoN}}^{\mathrm{App}} &= k_{\mathrm{PtoN}}\beta_{\mathrm{PtoN}}Q_{k_{\mathrm{PtoN}}}^{\frac{T-37.5}{10}} \end{aligned} \tag{A6}$$

The active force from cross-bridging (F_{XB}) is then scaled by the thick filament overlap fraction, $F_{\mathrm{act}} = \mathrm{OV}_{\mathrm{thick}}F_{XB}$. F_{XB} is calculated as

$$\begin{aligned} F_{XB}(t) = k_{\mathrm{stiff},1}&\left(\int_{-\infty}^{\infty} sp_2(t,s)ds + \int_{-\infty}^{\infty} sp_3(t,s)ds\right) \\ &+ k_{\mathrm{stiff},2}\Delta r\int_{-\infty}^{\infty} p_3(t,s)ds \end{aligned} \tag{A7}$$

where $p_2(t,s)$ is the probability density of strain s of actin-myosin cross-bridges bound in the pre-power-stroke configuration at time t, $p_3(t,s)$ is the probability density of strain s of actin-myosin cross-bridges bound in the post-power-stroke configuration at time t, and Δr is the displacement associated with the power stroke. $k_{\mathrm{stiff},2}$, the myosin head stiffness, controls the maximum myofilament force and $k_{\mathrm{stiff},1}$ is the stiffness of frictional forces from myosin-actin interaction.

Passive forces from titin and collagen are calculated using the constitutive model of Rice et al. [26]

$$\begin{aligned} F_{\mathrm{pas}} = \sigma_0(&P\mathrm{Con}_{\mathrm{titin}}(e^{P\exp_{\mathrm{titin}}(\mathrm{SL}-\mathrm{SL}_{\mathrm{rest}})} - 1) \\ &+ H(\mathrm{SL} - \mathrm{SL}_{\mathrm{collagen}})P\mathrm{Con}_{\mathrm{collagen}}(e^{P\exp_{\mathrm{collagen}}(\mathrm{SL}-\mathrm{SL}_{\mathrm{collagen}})} - 1) \end{aligned} \tag{A8}$$

where σ_{pas} is the passive stress, σ_0 is a scaling factor, $P\mathrm{Con}_{\mathrm{titin}}$ is the passive force contribution of titin, $P\exp_{\mathrm{titin}}$ is the mechanical nonlinearity of titin, SL is the sarcomere length, $\mathrm{SL}_{\mathrm{rest}}$ is the unloaded sarcomere length, $H(x)$ is the Heaviside step function, $\mathrm{SL}_{\mathrm{collagen}}$ is the unloaded collagen fiber length, $P\mathrm{Con}_{\mathrm{collagen}}$ is the passive force contribution of collagen, and $P\exp_{\mathrm{collagen}}$ is the mechanical nonlinearity of collagen.

The myofiber mechanics are then governed by conservation of momentum

$$\frac{dSL}{dt} = \frac{-F_{\mathrm{act}} - F_{\mathrm{pas}} + F_{\mathrm{SE}}}{\eta} \tag{A9}$$

F_{act} is the actin-myosin active force, F_{pas} is the passive force, F_{SE} is a corrective force for sarcomere length, and η is the myofiber viscosity.

Force-Dependent TrpC-Ca2+ Unbinding. Low and high affinity calcium binding (CaL, CaH) are calculated as

$$\begin{aligned} \frac{d\mathrm{CaL}}{dt} &= k_{\mathrm{on}}Q_{k_{\mathrm{on}}}^{\frac{T-37.5}{10}}[\mathrm{Ca}^{2+}](1 - \mathrm{CaL}) - f(\sigma)k_{\mathrm{off}L}Q_{k_{\mathrm{off}}}^{\frac{T-37.5}{10}} \\ \frac{d\mathrm{CaH}}{dt} &= k_{\mathrm{on}}Q_{k_{\mathrm{on}}}^{\frac{T-37.5}{10}}[\mathrm{Ca}^{2+}](1 - \mathrm{CaH}) - f(\sigma)k_{\mathrm{off}H}Q_{k_{\mathrm{off}}}^{\frac{T-37.5}{10}} \end{aligned} \tag{A10}$$

K_{on} is the binding rate of Ca^{2+} to TrpC, while $k_{\mathrm{off}L}$ and $k_{\mathrm{off}H}$ are unbinding rates. $f(\sigma)$ is a factor for the force-dependent unbinding of Ca^{2+} from TrpC

$$f(\sigma) = 1 - \zeta\frac{F_{XB}}{F_{XB}^{\max}} \tag{A11}$$

ζ is a scaling factor, while $F_{XB}^{\max}$ is the theoretical maximum cross-bridging force calculated from the King-Altman enzyme kinetics method

$$F_{XB}^{\max} = k_{\mathrm{stiff},2}\Delta r\frac{k_1k_2k_a}{k_1k_2k_3 + k_2k_3k_d + k_1k_2k_a + k_2k_3k_a + k_3k_{-1}k_d + k_1k_{-2}k_a + \cdots k_3k_{-1}k_a + k_{-1}k_{-2}k_d + k_{-1}k_{-2}k_{\mathrm{a}}} \tag{A12}$$

The kinetic rate constants are defined as in Ref. [28].

Biventricular Mechanics. A three-wall segment, biventricular mechanics model of Lumens et al. [29] is used for the heart. RV, LV, and septum myofibers are assumed to have identical properties unless otherwise noted. For each ventricle wall segment, the sarcomere length (L_s) is calculated for each ventricular segment using the natural strain (ϵ_f)

$$\begin{aligned} L_s &= L_{\text{rest}} e^{\epsilon_f} \\ \epsilon_f &\cong \frac{1}{2}\log\left(\frac{A_m}{A_{m,\text{ref}}}\right) - \frac{1}{12}z^2 - 0.019z^4 \\ z &= \frac{3C_m V_w}{2A_m} \\ V_m &= \frac{\pi}{6}x_m\left(x_m^2 + 3y_m^2\right) \\ A_m &= \pi\left(x_m^2 + y_m^2\right) \\ C_m &= \frac{2x_m}{x_m^2 + y_m^2} \end{aligned} \tag{A13}$$

A_m is the midwall surface area, ref refers to a reference unloaded geometry, C_m is the midwall curvature, and V_W is the wall segment volume. x_m and y_m thus determine the ventricular wall geometries.

Next, equilibrium of forces where the RV, LV wall, and septum meet must be achieved. Midwall tension is calculated as

$$T_m \cong \frac{V_w \lambda_{XB} F_{\text{act}}}{2A_m}\left(1 + \frac{z^2}{3} + \frac{z^4}{5}\right) \tag{A14}$$

where λ_{XB} is a scaling factor accounting for in vivo versus ex vivo myofiber contraction. T_m is used to compute perpendicular tension components

$$\begin{aligned} T_x &= T_m \sin\alpha \\ T_y &= T_m \cos\alpha \end{aligned} \tag{A15}$$

where $\sin\alpha = (2x_m y_m / x_m^2 + y_m^2)$ and $\cos\alpha = (-x_m^2 + y_m^2 / x_m^2 + y_m^2)$.

Then, RV and LV pressures are calculated as

$$\begin{aligned} P_{\text{LV}} &= -\frac{2T_{x,\text{LW}}}{y_{m,\text{LW}}} \\ P_{\text{RV}} &= \frac{2T_{x\text{RW}}}{y_{m,\text{RW}}} \end{aligned} \tag{A16}$$

Finally, x_m and y_m are adjusted so

$$\begin{aligned} V_{m,\text{LW}} &= -V_{\text{LV}} - \frac{1}{2}V_{w,\text{LW}} - \frac{1}{2}V_{w,\text{SW}} + V_{m,\text{SW}} \\ V_{m,\text{RW}} &= V_{\text{RV}} - \frac{1}{2}V_{w,\text{RW}} - \frac{1}{2}V_{w,\text{SW}} - V_{m,\text{SW}} \\ \Sigma T_x &= 0, \quad \Sigma T_y = 0 \end{aligned} \tag{A17}$$

Circulations. Lumped parameter models are used to simulate systemic and pulmonary hemodynamics. The total circulation has five compartments: pulmonary artery, pulmonary vein, systemic arteries, systemic veins, and the aorta. Compartment pressure is

$$P = \frac{V}{C} \tag{A18}$$

Flow between compartments is calculated as

$$Q = \frac{P_1 - P_2}{R} \tag{A19}$$

and compartment volume is then defined through its time derivative

$$\frac{dV}{dt} = Q_{\text{in}} - Q_{\text{out}} \tag{A20}$$

For valves, the flowrate is constrained to be positive, i.e., $Q = \max((P_1 - P_2/R), 0)$.

To better capture ventricular filling and preload, a varying compliance atrial model [45] was incorporated. The atrial pressure is calculated as

$$P_{\text{atria}} = \frac{V_{\text{atria}}}{C_{\text{atria}}} \tag{A21}$$

where P_{atria} is the atrial pressure, C_{atria} is the atrial compliance, and V_{atria} is the atrial volume. The time-varying compliance is shown in Fig. 8, where $C_{\max}$ and $C_{\min}$ are the maximum and minimum atrial compliances, respectively, and t_{start}, t_{peak}, and t_{end} are the time in a heartbeat when atrial contraction begins, is maximum, and ceases, respectively. These times along with the maximum and minimum atrial compliances ($C_{\max}$, $C_{\min}$) are consistent for all simulations, both baseline and pathological.

Parameter Estimation. Myofiber mechanics parameters were previously estimated [28] from rat cardiac muscle sinusoidal length perturbation experiments (frequencies 0.125–100 Hz) for varied [ATP] (0.4–5 mM) and [Pi] (0–4 mM) by minimizing the error function

$$\min_\theta E(\theta), E(\theta) = \sum_i^{N_{\text{Exp}}}\sum_j^{N_{\text{freq}}} \frac{1}{N_{\text{freq}}} \frac{\left(X_{i,j}^{\text{data}} - X_{i,j}^{\text{model}}(\theta)\right)^2}{\sigma(X)_{i,j}^2} \tag{A22}$$

using the PIKAIA genetic algorithm [46]. N_{exp} is the number of varied [ATP] and [Pi] experiments and N_{freq} is the number of frequencies over which experiments were performed. $X_{i,j}^{\text{data}}$ and $X_{i,j}^{\text{model}}$ are the experimental or simulated, elastic and viscous moduli for frequency j in experiment i, and $\sigma(X)_{i,j}^2$ is the experimental variance. Estimated myofiber parameters were validated by simulating experiments to which the parameters were not fit [28].

Circulatory resistance values were calculated directly from experimental hemodynamic data [27], while the compliances and three ventricular reference midwall areas were fit to rat hemodynamic data [27].

Simulation Convergence. In order to ensure that the cardiovascular system reached a steady-state solution, simulations were run until the convergence criteria, RV and LV stroke volume difference less than 2%, were met. Convergence usually occurred after approximately 200 heartbeats. Simulations were performed with a variable-step, variable-order solver for stiff differential-algebraic systems (ode15 s in MATLAB R2017a). The relative error tolerance was set to 1×10^{-8} and the absolute error tolerance was set to 1×10^{-10}.

Baseline Model Parameters. See Table 4.

Table 4 Baseline model parameters

Parameter	Description	Value	Reference
Thick-thin filament activation parameters			
L_{thick}	Length of thick filament	1.67 μm	Gordon et al. [47]
L_{thin}	Length of thin filament	1.2 μm	Rice et al. [26]
L_{bare}	Length of bare region of thick filament	0.1 μm	Rice et al. [26]
k_{on}	Association rate of Ca^{2+} with TrpC	100 μM	Niederer et al. [48]
k_{offL}	Dissociation rate of Ca^{2+} from low affinity TrpC	4218.5 s^{-1}	Tewari et al. [6]
k_{offH}	Dissociation rate of Ca^{2+} from high affinity TrpC	156.5 s^{-1}	Tewari et al. [6]
Z	Force sensitivity of Ca^{2+} unbinding rate	0.23	Tewari et al. [6]
β_{50}	TrpReg value which the effect is half-maximal	0.5	Rice et al. [26]
n_β	Hill-coefficient of the TrpReg effect	15	Rice et al. [26]
Q_{kon}	Temperature dependence of k_{on}	1.5	Rice et al. [26]
Q_{koff}	Temperature dependence of k_{off}	1.3	Rice et al. [26]
Cross-bridge cycling parameters			
k_{np}	Transition rate from N to P	329.2 s^{-1}	Tewari et al. [6]
k_{pn}	Transition rate from P to N	50 s^{-1}	Rice et al. [26]
k_a	Myosin-actin rate of attachment	294.1 s^{-1}	Tewari et al. [28]
k_d	Myosin-actin rate of detachment	88.9 s^{-1}	See footnote[a]
k_1	Transition rate from $A_1{}^T$ to $A_2{}^T$	10.2 s^{-1}	Tewari et al. [28]
k_{-1}	Transition rate from $A_2{}^T$ to $A_1{}^T$	10.3 s^{-1}	Tewari et al. [28]
K_2	Transition rate from $A_2{}^T$ to $A_3{}^T$	88.6 s^{-1}	Tewari et al. [28]
k_{-2}	Transition rate from $A_3{}^T$ to $A_2{}^T$	20.9 s^{-1}	See footnote[b]
k_3	Transition rate from A_3 to P	35.6 s^{-1}	Tewari et al. [28]
α_1	Stretch sensing parameter for k_1 and k_{-1}	10 μm^{-1}	Tewari et al. [28]
α_2	Stretch sensing parameter for k_2 and k_{-2}	9 μm^{-1}	Tewari et al. [28]
α_3	Stretch sensing parameter for k_3	59.3 μm^{-1}	Tewari et al. [28]
s_3	Strain at which k_3 is minimum	9.9 nm	Tewari et al. [28]
$k_{stiff,1}$	Stiffness of frictional forces arising due to myosin-actin interaction	2827.1 kPa μm^{-1}	Tewari et al. [28]
$k_{stiff,2}$	Stiffness of forces arising due to cross-bridge powerstroke	51,871 kPa μm^{-1}	Tewari et al. [28]
Q_{kNtoP}	Temperature dependence of k_{NtoP}	1.6	Rice et al. [26]
Q_{kPtoN}	Temperature dependence of k_{PtoN}	1.6	Rice et al. [26]
$Q_{XB,1}$	Temperature dependence of k_a, k_1	3.82	Tewari et al. [6]
$Q_{XB,2}$	Temperature dependence of k_d, k_{-1}	2.39	Tewari et al. [6]
$Q_{XB,3}$	Temperature dependence of k_2, k_3	6.73	Tewari et al. [6]
$Q_{XB,4}$	Temperature dependence of $k_{stiff,1}$	1.34	Tewari et al. [28]
$Q_{XB,5}$	Temperature dependence of $k_{stiff,2}$	1.44	Tewari et al. [28]
Other myofiber parameters			
λ_{XB}	Factor scaling cross-bridge force	1.31	Tewari et al. [28]; See Footnote[c]
K_{SE}	Stiffness of series element	1000 kPa μm^{-1}	Tewari et al. [6]
η	Viscosity coefficient of cardiac muscle	1 kPa s μm^{-1}	Tewari et al. [6]
Passive force generation			
SL_{rest}	Resting sarcomere length	1.9 μm	Rice et al. [26]
$PCon_{titin}$	Contribution of titin	0.002 (Normalized force)	Rice et al. [26]
$PExp_{titin}$	Expression of titin	10 unitless	Rice et al. [26]
$PCon_{collagen}$	Contribution of collagen	0.02 (Normalized force)	Rice et al. [26]
$PExp_{collagen}$	Expression of collagen	70 unitless	Rice et al. [26]
$SL_{collagen}$	Threshold for collagen activation	2.25 μm	Rice et al. [26]
Σpas	Maximum passive stress	7 kPa	Lumens et al. [29]
Circulatory parameters			
R_{PV}	Pulmonary vasculature resistance	19.2 mmHg s mL^{-1}	Tewari et al. [6]
R_{SV}	Systemic vasculature resistance	117.6 mmHg s mL^{-1}	Tewari et al. [6]
R_{Ao}	Aortic resistance	1.96 mmHg s mL^{-1}	Tewari et al. [6]
C_{Ao}	Aortic compliance	0.00015 mL $mmHg^{-1}$	Tewari et al. [6]
C_{SA}	Systemic artery compliance	0.0035 mL $mmHg^{-1}$	Tewari et al. [6]
C_{SV}	Systemic vein compliance	19.33 mL $mmHg^{-1}$	Tewari et al. [6]
C_{PA}	Pulmonary artery compliance	2.42 mL $mmHg^{-1}$	Tewari et al. [6]
C_{PV}	Pulmonary vein compliance	0.009 mL $mmHg^{-1}$	Tewari et al. [6]
Varying compliance atria parameters			
$C_{atria,max}$	Maximum atrial compliance	4 mL $mmHg^{-1}$	Fit to Reil et al. [49]
$C_{atria,min}$	Minimum atrial compliance	0.2 mL $mmHg^{-1}$	Fit to Reil et al. [49]
T_{peak}	Time in heartbeat with maximum atrial contraction	23 ms	Fit to Reil et al. [49]
T_{end}	Time in heartbeat when atrial contraction ends	44 ms	Fit to Reil et al. [49]
T_{start}	Time in heartbeat when atrial contraction starts	129 ms	Fit to Reil et al. [49]
TriSeg parameters			
$V_{w,lw}$	LV wall volume	0.4653 mL	Tewari et al. [6]
$V_{w,sw}$	Septal wall volume	0.2506 mL	Tewari et al. [6]
$V_{w,rw}$	RV wall volume	0.1933 mL	Tewari et al. [6]

Table 4 (continued)

Parameter	Description	Value	Reference
$ALW_{m,ref}$	LV midwall reference surface area	1.38 cm^2	Tewari et al. [6]
$ASW_{m,ref}$	Septal midwall reference surface area	0.78 cm^2	Tewari et al. [6]
$ARW_{m,ref}$	RV midwall reference surface area	2.18 cm^2	Tewari et al. [6]

[a]Scaled by 2.5 factor so k_d/k_a matches mouse values [28]. Experimental data not available in rats.
[b]Scaled by 10 factor so k_{-2} is of a similar magnitude to k_2 [28]. Experimental data were not available.
[c]Scaling factor to account for myofilament force generation in vivo versus in vitro [28].

References

[1] Hosenpud, J. D., Bennett, L. E., Keck, B. M., Boucek, M. M., and Novick, R. J., 2000, "The Registry of the International Society for Heart and Lung Transplantation: Seventeenth Official Report-2000," J. Heart. Lung Transplant., **19**(10), pp. 909–931.

[2] Ghio, S., Gavazzi, A., Campana, C., Inserra, C., Klersy, C., Sebastiani, R., Arbustini, E., Recusani, F., and Tavazzi, L., 2001, "Independent and Additive Prognostic Value of Right Ventricular Systolic Function and Pulmonary Artery Pressure in Patients With Chronic Heart Failure," J. Am. Coll. Cardiol., **37**(1), pp. 183–188.

[3] Friedberg, M. K., and Redington, A. N., 2014, "Right Versus Left Ventricular Failure: Differences, Similarities, and Interactions," Circulation, **129**(9), pp. 1033–1044.

[4] Vonk Noordegraaf, A., and Galie, N., 2011, "The Role of the Right Ventricle in Pulmonary Arterial Hypertension," Eur. Respir. Rev., **20**(122), pp. 243–253.

[5] Sztrymf, B., Souza, R., Bertoletti, L., Jaïs, X., Sitbon, O., Price, L. C., Simonneau, G., and Humbert, M., 2010, "Prognostic Factors of Acute Heart Failure in Patients With Pulmonary Arterial Hypertension," Eur. Respir. J., **35**(6), pp. 1286–1293.

[6] Tewari, S. G., Bugenhagen, S. M., Vinnakota, K. C., Rice, J. J., Janssen, P. M. L., and Beard, D. A., 2016, "Influence of Metabolic Dysfunction on Cardiac Mechanics in Decompensated Hypertrophy and Heart Failure," J. Mol. Cell Cardiol., **94**, pp. 162–175.

[7] Bers, D. M., 2000, "Calcium Fluxes Involved in Control of Cardiac Myocyte Contraction," Circ. Res., **87**(4), pp. 275–281.

[8] Ventura-Clapier, R., Garnier, A., Veksler, V., and Joubert, F., 2011, "Bioenergetics of the Failing Heart," Biochim. Biophys. Acta, **1813**(7), pp. 1360–1372.

[9] Golob, M., Moss, R. L., and Chesler, N. C., 2014, "Cardiac Tissue Structure, Properties, and Performance: A Materials Science Perspective," Ann. Biomed. Eng., **42**(10), pp. 2003–2013.

[10] Tabima, D. M., Philip, J. L., and Chesler, N. C., 2017, "Right Ventricular-Pulmonary Vascular Interactions," Physiol. (Bethesda), **32**(5), pp. 346–356.

[11] Buckberg, G., Mahajan, A., Saleh, S., Hoffman, J. I., and Coghlan, C., 2008, "Structure and Function Relationships of the Helical Ventricular Myocardial Band," J. Thorac. Cardiovasc. Surg., **136**(3), pp. 578–589.

[12] Liu, A., Philip, J., Vinnakota, K. C., Van den Bergh, F., Tabima, D. M., Hacker, T., Beard, D. A., and Chesler, N. C., 2017, "Estrogen Maintains Mitochondrial Content and Function in the Right Ventricle of Rats With Pulmonary Hypertension," Physiol. Rep., **5**(6), p. e13157.

[13] Gomez-Arroyo, J., Mizuno, S., Szczepanek, K., Van Tassell, B., Natarajan, R., dos Remedios, C. G., Drake, J. I., Farkas, L., Kraskauskas, D., Wijesinghe, D. S., Chalfant, C. E., Bigbee, J., Abbate, A., Lesnefsky, E. J., Bogaard, H. J., and Voelkel, N. F., 2013, "Metabolic Gene Remodeling and Mitochondrial Dysfunction in Failing Right Ventricular Hypertrophy Secondary to Pulmonary Arterial Hypertension," Circ. Heart Fail., **6**(1), pp. 136–144.

[14] Bache, R. J., Zhang, J., Murakami, Y., Zhang, Y., Cho, Y. K., Merkle, H., Gong, G., From, A. H., and Ugurbil, K., 1999, "Myocardial Oxygenation at High Workstates in Hearts With Left Ventricular Hypertrophy," Cardiovasc. Res., **42**(3), pp. 616–626.

[15] Cowley, P. M., Wang, G. Y., Joshi, S. K., Swigart, P. M., Lovett, D. H., Simpson, P. C., and Baker, A. J., 2017, "α1A-Subtype Adrenergic Agonist Therapy for Failing Right Ventricle," Am. J. Physiol. Heart Circ. Physiol., **313**(6), pp. H1109–H1118.

[16] Wang, G. Y., Yeh, C. C., Jensen, B. C., Mann, M. J., Simpson, P. C., and Baker, A. J., 2010, "Heart Failure Switches the RV α1-Adrenergic Inotropic Response From Negative to Positive," Am. J. Physiol. Heart Circ. Physiol., **298**(3), pp. H913–H920.

[17] Rain, S., Andersen, S., Najafi, A., Gammelgaard Schultz, J., da Silva Goncalves Bos, D., Handoko, M. L., Bogaard, H. J., Vonk-Noordegraaf, A., Andersen, A., van der Velden, J., Ottenheijm, C. A., and de Man, F. S., 2016, "Right Ventricular Myocardial Stiffness in Experimental Pulmonary Arterial Hypertension: Relative Contribution of Fibrosis and Myofibril Stiffness," Circ. Heart Fail., **9**(7), pp. 1–9.

[18] Wang, Z., Patel, J. R., Schreier, D. A., Hacker, T. A., Moss, R. L., and Chesler, N. C., 2018, "Organ-Level Right Ventricular Dysfunction With Preserved Frank-Starling Mechanism in a Mouse Model of Pulmonary Arterial Hypertension," J. Appl. Physiol., (epub).

[19] Bogaard, H. J., Natarajan, R., Henderson, S. C., Long, C. S., Kraskauskas, D., Smithson, L., Ockaili, R., McCord, J. M., and Voelkel, N. F., 2009, "Chronic Pulmonary Artery Pressure Elevation is Insufficient to Explain Right Heart Failure," Circulation, **120**(20), pp. 1951–1960.

[20] Drake, J. I., Bogaard, H. J., Mizuno, S., Clifton, B., Xie, B., Gao, Y., Dumur, C. I., Fawcett, P., Voelkel, N. F., and Natarajan, R., 2011, "Molecular Signature of a Right Heart Failure Program in Chronic Severe Pulmonary Hypertension," Am. J. Respir. Cell Mol. Biol., **45**(6), pp. 1239–1247.

[21] Rain, S., Handoko, M. L., Vonk Noordegraaf, A., Bogaard, H. J., van der Velden, J., and de Man, F. S., 2014, "Pressure-Overload-Induced Right Heart Failure," Pflugers Arch., **466**(6), pp. 1055–1063.

[22] Vanderpool, R. R., Pinsky, M. R., Naeije, R., Deible, C., Kosaraju, V., Bunner, C., Mathier, M. A., Lacomis, J., Champion, H. C., and Simon, M. A., 2015, "RV-Pulmonary Arterial Coupling Predicts Outcome in Patients Referred for Pulmonary Hypertension," Heart, **101**(1), pp. 37–43.

[23] Territo, P. R., French, S. A., and Balaban, R. S., 2001, "Simulation of Cardiac Work Transitions, In Vitro: Effects of Simultaneous Ca^{2+} and ATPase Additions on Isolated Porcine Heart Mitochondria," Cell Calcium, **30**(1), pp. 19–27.

[24] Bazil, J. N., Beard, D. A., and Vinnakota, K. C., 2016, "Catalytic Coupling of Oxidative Phosphorylation, ATP Demand, and Reactive Oxygen Species Generation," Biophys. J., **110**(4), pp. 962–971.

[25] Zahalak, G. I., 1986, "A Comparison of the Mechanical Behavior of the Cat Soleus Muscle With a Distribution-Moment Model," ASME J. Biomech. Eng., **108**(2), pp. 131–140.

[26] Rice, J. J., Wang, F., Bers, D. M., and de Tombe, P. P., 2008, "Approximate Model of Cooperative Activation and Crossbridge Cycling in Cardiac Muscle Using Ordinary Differential Equations," Biophys. J., **95**(5), pp. 2368–2390.

[27] Tran, K., Smith, N. P., Loiselle, D. S., and Crampin, E. J., 2010, "A Metabolite-Sensitive, Thermodynamically Constrained Model of Cardiac Cross-Bridge Cycling: Implications for Force Development During Ischemia," Biophys. J., **98**(2), pp. 267–276.

[28] Tewari, S. G., Bugenhagen, S. M., Palmer, B. M., and Beard, D. A., 2016, "Dynamics of Cross-Bridge Cycling, ATP Hydrolysis, Force Generation, and Deformation in Cardiac Muscle," J. Mol. Cell Cardiol., **96**, pp. 11–25.

[29] Lumens, J., Delhaas, T., Kirn, B., and Arts, T., 2009, "Three-Wall Segment (TriSeg) Model Describing Mechanics and Hemodynamics of Ventricular Interaction," Ann. Biomed. Eng., **37**(11), pp. 2234–2255.

[30] Ben Driss, A., Devaux, C., Henrion, D., Duriez, M., Thuillez, C., Levy, B. I., and Michel, J. B., 2000, "Hemodynamic Stresses Induce Endothelial Dysfunction and Remodeling of Pulmonary Artery in Experimental Compensated Heart Failure," Circulation, **101**(23), pp. 2764–2770.

[31] Hemnes, A. R., Zaiman, A., and Champion, H. C., 2008, "PDE5A Inhibition Attenuates Bleomycin-Induced Pulmonary Fibrosis and Pulmonary Hypertension Through Inhibition of ROS Generation and RhoA/Rho Kinase Activation," Am. J. Physiol. Lung Cell Mol. Physiol., **294**(1), pp. L24–L33.

[32] Liu, A., Tian, L., Golob, M., Eickhoff, J. C., Boston, M., and Chesler, N. C., 2015, "17β-Estradiol Attenuates Conduit Pulmonary Artery Mechanical Property Changes With Pulmonary Arterial Hypertension," Hypertens., **66**(5), pp. 1082–1088.

[33] Jasmin, J. F., Mercier, I., Hnasko, R., Cheung, M. W., Tanowitz, H. B., Dupuis, J., and Lisanti, M. P., 2004, "Lung Remodeling and Pulmonary Hypertension After Myocardial Infarction: Pathogenic Role of Reduced Caveolin Expression," Cardiovasc. Res., **63**(4), pp. 747–755.

[34] Zhang, Y., Barocas, V. H., Berceli, S. A., Clancy, C. E., Eckmann, D. M., Garbey, M., Kassab, G. S., Lochner, D. R., McCulloch, A. D., Tran-Son-Tay, R., and Trayanova, N. A., 2016, "Multi-Scale Modeling of the Cardiovascular System: Disease Development, Progression, and Clinical Intervention," Ann. Biomed. Eng., **44**(9), pp. 2642–2660.

[35] Kerckhoffs, R. C., Campbell, S. G., Flaim, S. N., Howard, E. J., Sierra-Aguado, J., Mulligan, L. J., and McCulloch, A. D., 2009, "Multi-Scale Modeling of Excitation-Contraction Coupling in the Normal and Failing Heart," IEEE Engineering in Medicine and Biology Society (EMBC), Minneapolis, MN, Sept. 3–6, pp. 4281–4282.

[36] Garbey, M., Rahman, M., and Berceli, S. A., 2015, "A Multiscale Computational Framework to Understand Vascular Adaptation," J. Comput. Sci., **8**, pp. 32–47.

[37] Golob, M. J., Wang, Z., Prostrollo, A. J., Hacker, T. A., and Chesler, N. C., 2016, "Limiting Collagen Turnover Via Collagenase-Resistance Attenuates Right Ventricular Dysfunction and Fibrosis in Pulmonary Arterial Hypertension," Physiol. Rep., **4**(11), p. e12815.

[38] Lahm, T., Frump, A. L., Albrecht, M. E., Fisher, A. J., Cook, T. G., Jones, T. J., Yakubov, B., Whitson, J., Fuchs, R. K., Liu, A., Chesler, N. C., and Brown, M. B., 2016, "17β-Estradiol Mediates Superior Adaptation of Right Ventricular Function to Acute Strenuous Exercise in Female Rats With Severe Pulmonary Hypertension," Am. J. Physiol. Lung Cell Mol. Physiol., **311**(2), pp. L375–L388.

[39] Costandi, P. N., Frank, L. R., McCulloch, A. D., and Omens, J. H., 2006, "Role of Diastolic Properties in the Transition to Failure in a Mouse Model of the

Cardiac Dilatation," Am. J. Physiol. Heart Circ. Physiol., **291**(6), pp. H2971–H2979.
[40] Hill, M. R., Simon, M. A., Valdez-Jasso, D., Zhang, W., Champion, H. C., and Sacks, M. S., 2014, "Structural and Mechanical Adaptations of Right Ventricle Free Wall Myocardium to Pressure Overload," Ann. Biomed. Eng., **42**(12), pp. 2451–2465.
[41] Avazmohammadi, R., Hill, M. R., Simon, M. A., Zhang, W., and Sacks, M. S., 2017, "A Novel Constitutive Model for Passive Right Ventricular Myocardium: Evidence for Myofiber-Collagen Fiber Mechanical Coupling," Biomech. Model. Mechanobiol., **16**(2), pp. 561–581.
[42] Wu, F., Zhang, E. Y., Zhang, J., Bache, R. J., and Beard, D. A., 2008, "Phosphate Metabolite Concentrations and ATP Hydrolysis Potential in Normal and Ischaemic Hearts," J. Physiol., **586**(17), pp. 4193–4208.
[43] Wu, F., Zhang, J., and Beard, D. A., 2009, "Experimentally Observed Phenomena on Cardiac Energetics in Heart Failure Emerge From Simulations of Cardiac Metabolism," Proc. Natl. Acad. Sci. U. S. A., **106**(17), pp. 7143–7148.
[44] Palmer, B. M., 2010, "A Strain-Dependency of Myosin Off-Rate Must be Sensitive to Frequency to Predict the B-Process of Sinusoidal Analysis," Adv. Exp. Med. Biol., **682**, pp. 57–75.
[45] Lu, K., Clark, J. W., Ghorbel, F. H., Ware, D. L., and Bidani, A., 2001, "A Human Cardiopulmonary System Model Applied to the Analysis of the Valsalva Maneuver," Am. J. Physiol. Heart Circ. Physiol., **281**(6), pp. H2661–H2679.
[46] Charbonneau, P., 2002, "An Introduction to Genetic Algorithms for Numerical Optimization," National Center for Atmospheric Research, Boulder, CO, Technical Note https://www.researchgate.net/publication/228608597_An_Introduction_to_Genetic_Algorithms_for_Numerical_Optimization
[47] Gordon, A. M., Huxley, A. F., and Julian, F. J., 1966, "The Variation in Isometric Tension With Sarcomere Length in Vertebrate Muscle Fibres," J. Physiol., **184**(1), pp. 170–192.
[48] Niederer, S. A., Hunter, P. J., and Smith, N. P., 2006, "A Quantitative Analysis of Cardiac Myocyte Relaxation: A Simulation Study," Biophys. J., **90**(5), pp. 1697–722.
[49] Reil, J. C., Hohl, M., Selejan, S., Lipp, P., Drautz, F., Kazakow, A., Münz, B. M., Müller, P., Steendijk, P., Reil, G. H., Allessie, M. A., Böhm, M., and Neuberger, H. R., 2012, "Aldosterone Promotes Atrial Fibrillation," Eur. Heart J., **33**(16), pp. 2098–2108.